Acta Crystallographica Section B
Structural Science
ISSN 0108-7681

Polymorphism and piezochromicity in the three-dimensional network-based phosphate $RbCuPO_4$

Paul F. Henry,* Simon A. J. Kimber and Dimitri N. Argyriou

MI-1, Helmholtz Zentrum Berlin für Materialien und Energie, Hahn-Meitner-Platz 1, 14109, Berlin, Germany

Correspondence e-mail: paul.henry@helmholtz-berlin.de

Received 23 March 2010
Accepted 31 May 2010

Rubidium copper phosphate, $RbCuPO_4$, forms two room-temperature polymorphs that have been investigated with neutron powder diffraction. Polymorph (II) can be converted quantitatively into (I) by grinding the material or by pelletization, and the phase transition is accompanied by a significant colour change from very pale green to sky blue. Polymorph (II) can be obtained essentially free of (I) by quenching from 723 K. Each polymorph shows two unique Cu atoms: in (I) both sites are four-coordinate in a 2:1 ratio, whereas in (II) the atoms are four- and five-coordinate in a 1:1 ratio. In each case these sites are linked by phosphate tetrahedra to form three-dimensional frameworks based on the $4^2 6^3 8$-*a* four-connected net. The Rb atoms are hosted in the six- and eight-ring channels that are similar to those observed in zeolite ABW. The (II) $\rightarrow$ (I) phase transition is also accompanied by a volume reduction of 2.1% even though the average coordination of the Cu atoms also falls. The structures of the polymorphs are critically examined and compared with those of $KNiPO_4$ and $KCuPO_4$ in terms of hexagonal close packing containing ordered phosphate arrays. As a result of buckling of the six-ring layers, one-dimensional chains of dimerized copper polyhedra are identified in (II), chains that become trimers with mirror symmetry in (I).

1. Introduction

Phosphate-based frameworks incorporating transition metals show a variety of interesting properties (catalysts, pigments, fast ion conductors) and are candidate materials for use in solid oxide fuel cells, while they also have the potential to exhibit novel magnetic ordering; both fields of considerable interest over the last decade. Aluminophosphates and doped analogues were the first to be considered because $[PO_4]^{3-}$ is isoelectronic to $[SiO_4]^{4-}$, the structural moiety that is the basic building block for aluminosilicate zeolite structures. There have been considerable efforts to prepare other phosphate-based framework structures containing transition metals due to the flexibility of the framework materials, allowing different valence and/or coordination numbers. Zeotype structures that permit a high degree of transition metal substitution are usually dense (in terms of tetrahedral units per unit volume) and are dominated by the ABW, CAS, ANA and BIK framework families (Baerlocher & McCusker, 1996) that lie very close to the boundary between zeolites and conventional oxide materials (Weller, 2000). Materials with a 1:1 ratio of transition metal to phosphate that retain one of the zeolite structure classes are relatively rare and are dominated by first-row transition metals that have appreciable tetrahedral coordination chemistry with oxygen, such as Co^{2+} and Zn^{2+} (*e.g.* Bu *et al.*, 1997; Chippindale *et al.*, 1999; Harrison, 2000).

Phosphates containing Mn, Fe, Ni and Cu in the 2+ oxidation state are known, but almost all are variants of the olivine structure, which can be described as a collapsed framework driven by an increase in the coordination number of the transition metal (Corbridge, 1973).

Materials that show magnetoelectric (ME) properties have been the subject of intense interest in recent years (Eerenstein *et al.*, 2006; Khomskii, 2006; Cheong & Mostovoy, 2007). Recently, the nickel-based phosphate $LiNiPO_4$ (with the olivine structure) was shown to exhibit field-induced magnetic phases and electric polarization (Jensen, Christensen, Kenzelmann, Rønnow, Niedermayer, Andersen, Lefmann, Jiménez-Ruiz *et al.*, 2009; Jensen, Christensen, Kenzelmann, Rønnow, Niedermayer, Andersen, Lefmann, Schefer *et al.*, 2009). While all the alkali metal orthophosphates (Li, Na, K) show low-temperature commensurate antiferromagnetic (AF) phases, only $LiNiPO_4$ exhibits a commensurate (C)–incommensurate (IC) AF phase transition (Vaknin *et al.*, 2004), illustrating the role of the group (I) cation in determining the magnetic properties. Additionally, there have been several reports of incorporation of Cu^{2+} into framework materials based on arrays of [CuO] square-planar trimers that show geometrically induced magnetic phenomena (Mo *et al.*, 2006; Ranmohotti *et al.*, 2006). We have also previously described the incorporation of high levels of Cu^{2+} and Ni^{2+} into variants of the ABW zeolite structure containing distorted CuO_4 tetrahedra and NiO_5 square-based pyramids, although no magnetic properties were published at the time (Henry, Hughes *et al.*, 2000; Henry, Weller & Hughes, 2000).

Here we revisit the copper-based framework $RbCuPO_4$ using neutron powder diffraction as a precursor to evaluating the magnetic properties, showing that the structure of the orthorhombic polymorph is more complex than originally published. Additionally, the structure of the second reported monoclinic polymorph (Henry, Hughes *et al.*, 2000) has been solved in the $KCuPO_4$ structure type, also based on the same topological network as zeolite ABW. The two structures are critically compared and the structural origin of the observed piezochromic phase transition on grinding identified. The second polymorph shows structural features that could give rise to one-dimensional magnetism based on spin 1/2 chains, a topic of great current interest.

2. Experimental

Polycrystalline $RbCuPO_4$ was synthesized using soft chemistry techniques followed by low-temperature firing owing to the high volatility of the rubidium source. Stoichiometric amounts of $Cu(NO_3)_2{\cdot}2.5H_2O$ (Aldrich, 99.9%) and $NH_4H_2PO_4$ (Aldrich, 99%) were separately dissolved in deionized high resistivity water (18.2 MW) with the addition of a few ml of concentrated nitric acid. The solutions were mixed and further acid added until full dissolution occurred. Then 50 ml of ethanol was added, followed by the dropwise introduction of a 5% excess of RbOH (Aldrich, 50% solution by weight in water). Precipitation was seen to occur on the addition of the RbOH solution. The pH was slowly raised by the addition of ammonia solution until the precipitate redissolved. The resulting solution was slowly evaporated to dryness and then

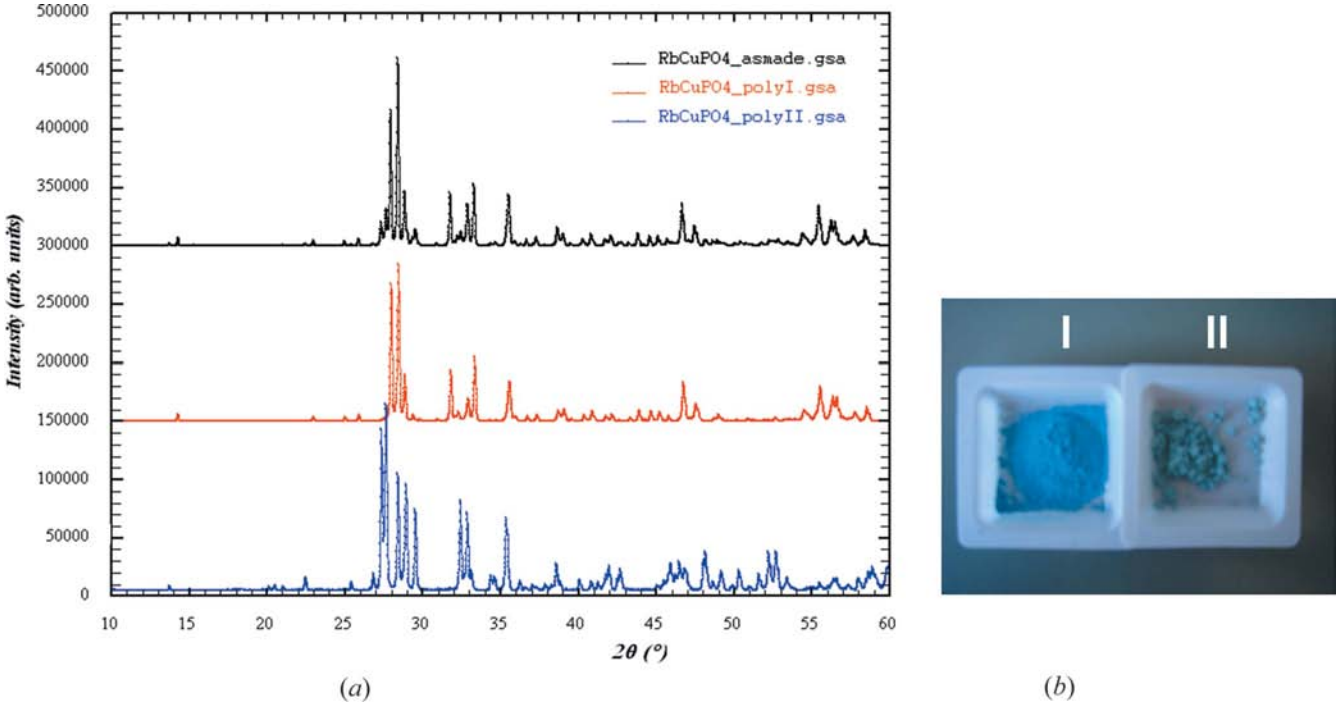

Figure 1
Powder X-ray diffraction patterns of as-made $RbCuPO_4$ (upper), after pelletization (middle) and after quenching from 723 K (lower) showing the co-existence of polymorphs (I) and (II) at room temperature. The inset shows the marked colour change of the two polymorphs.

decomposed over 12 h in a furnace by slow heating to 523 K. The resulting powder was thoroughly ground in an agate pestle and mortar before being fired at 923 K and then 1023 K, each for 12 h with an intermediate regrinding. Soluble impurities were then removed by washing thoroughly with deionized water under suction filtration followed by a final 12 h firing at 1023 K with furnace cooling back to room temperature.

X-ray powder diffraction patterns for preliminary phase characterization were collected using a Bruker D8 Advance diffractometer (Cu K radiation) operating with a Lynx-Eye energy discriminating position sensitive detector (PSD) to remove the $K\beta$ component. Neutron powder diffraction (NPD) data were collected using the high-resolution diffractometer E9 (Többens *et al.*, 2001) at the BER-II reactor in Berlin using 1.80 and 2.82 Å incident wavelengths from the focusing germanium monochromator under ambient conditions. Room-temperature data for polymorph (I) were also collected on D20 at the Institut Laue–Langevin in its high takeoff angle setting (Hansen *et al.*, 2008) using incident wavelengths of 1.87 [Ge(115)] and 1.36 Å [Ge(117)] to ensure a sufficient q range for an unconstrained Rietveld refinement. All refinements were carried out using the *GSAS* package of Rietveld software (Larson & Von Dreele, 1994) with the EXPGUI interface (Toby, 2001). Experimental details are given in Table 1.

2.1. Pre-characterization

Inspection of the X-ray powder diffraction (XPD) pattern of the as-synthesized material showed two phases were present, phases that could be indexed satisfactorily using an orthorhombic unit cell with a = 8.5261 (4), b = 5.3562 (3) and c = 8.9064 (4) Å [polymorph (I)] and a monoclinic cell with a = 5.0424 (8), b = 8.5880 (2), c = 9.6434 (2) Å and β = 91.51 (1)° [polymorph (II)], illustrated in Fig. 1 (upper) as previously reported (Henry, Hughes *et al.*, 2000). Both unit cells are consistent with the ABW-type framework (Bu *et al.*, 1997). Grinding caused a noticeable colour change to a brighter blue and, after pelletization under 5 tonnes for 5 min, only (I) was observed (Fig. 1*a*, middle). By modifying the cooling rate it was found that (II) could be isolated [essentially free of (I) from laboratory XPD data] by quenching the sample from 723 K (Fig. 1*a*, lower). Polymorph (II) was very pale green in bulk form, whereas (I) was sky blue, as shown in the inset to Fig. 1. The change in colour between the polymorphs was a clue that the phase transition involved a significant change in the environment of the colour centre.

2.2. Structure of polymorph (I)

Our previously published structure from XPD data (Henry, Hughes *et al.*, 2000), which contains a single copper site with flattened tetrahedral geometry, was used to model the NPD data from E9 and D20 in the polar space group $Pc2_1n$. This cell, however, did not account for a significant number of NPD reflections. Close inspection of the published XPD data showed that the fit statistics were relatively poor (R_{F^2} of 0.1706 for 315 observations). XPD data were collected using the high-count-rate Lynx-Eye detector and several weak low-angle diffraction peaks that did not correspond to any known impurities or starting materials were observed. Extraction and indexing of the weak XPD peaks and the non-fitted low-angle peaks in the NPD data yielded a tripled cell in the **b** direction, suggesting some ordering phenomenon was responsible for the supercell reflections based on the oxygen substructure, reflections that had been missed in the original X-ray data only refinement. A new model was constructed using the same space group and refined against the original XPD data, giving an R_{F^2} of < 0.09 for 823 observations. However, refinement of this model using the NPD data required soft constraints on bond distances and angles in order to converge, even with isotropic atomic displacement parameters (ADPs). This model required 21 atoms in the asymmetric unit compared with 7 in the original cell and predicted a number of weak low-angle reflections in the XPD and NPD patterns, reflections that were absent experimentally. A full systematic absence study was then performed using the supercell lattice constants and both the XPD and NPD data. Two possible space groups satisfied the observed reflection class

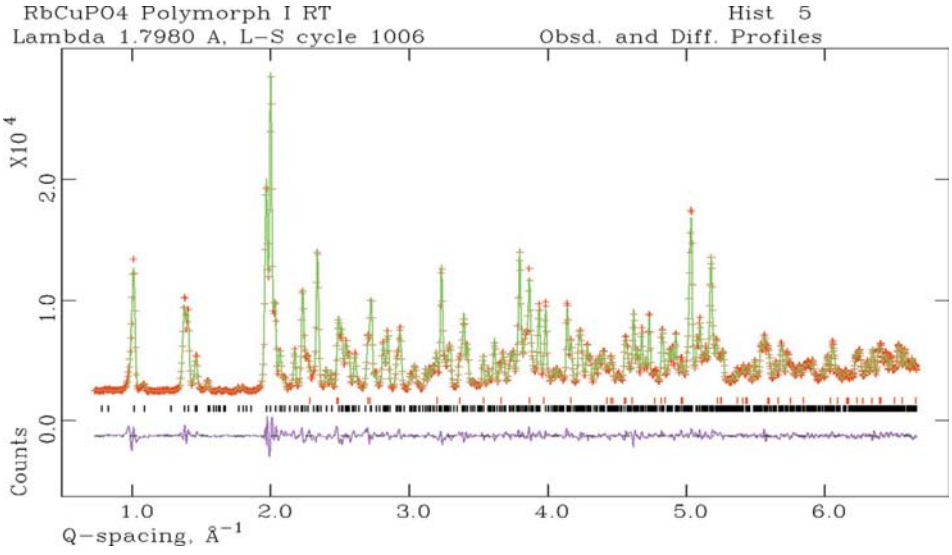

Figure 2
Final Rietveld refinement profile for the 1.80 Å incident wavelength E9 NPD data for $RbCuPO_4$ polymorph (I). The observed data are crosses, the calculated pattern a solid line, the tick marks show the allowed reflections (upper CuO) and the lower solid line is the difference plot; R_{wp} = 0.0383, R_p = 0.0291 and R_{F^2} = 0.0292 for 885 observations.

Table 1
Experimental details.

	(I)	(II)
Crystal data		
Chemical formula	$RbCuPO_4$	$RbCuPO_4$
M_r	243.985	243.985
Crystal system, space group	Orthorhombic, *Pnma*	Monoclinic, $P2_1$
Temperature (K)	293	293
a, *b*, *c* (Å)	8.93178 (24), 16.1181 (4), 8.56656 (23)	8.60296 (25), 9.65930 (26), 5.05388 (15)
β	90	91.422 (2)
V (Å^3)	1233.27 (6)	419.84 (2)
Z	12	4
Radiation type	Neutron variable wavelength, λ = 1.80, 2.82 Å (E9); 1.87, 1.36 Å (D20)	Neutron variable wavelength, λ = 1.80, 2.82 Å
Specimen shape, size (cm)	Powder, 1.2 × 1.2 × 3.5 (E9) 0.9 × 0.9 × 3.5 (D20)	Powder, 1.2 × 1.2 × 3.5
Data collection		
Diffractometer	D20 powder diffractometer, ILL, France (high takeoff angle option) E9 high-resolution powder diffractometer, BER II reactor, Berlin	E9 high-resolution powder diffractometer, BER II reactor, Berlin
Specimen mounting	Vanadium can (12 mm external diameter E9, 9 mm external diameter D20)	Vanadium can (12 mm external diameter)
Data collection mode	Transmission	Transmission
Scan method	Step (E9), continuous (D20)	Step
2θ values (°)	$2\theta_{min}$ = 6, $2\theta_{max}$ = 143, $2\theta_{step}$ = 0.078 (E9) $2\theta_{min}$ = 10, $2\theta_{max}$ = 140, $2\theta_{step}$ = 0.1 (D20)	$2\theta_{min}$ = 6, $2\theta_{max}$ = 143, $2\theta_{step}$ = 0.078
Refinement		
R factors	R_p = 0.021, R_{wp} = 0.0292, R_{F^2} = 0.0175, 790 observations (1.87 Å D20) R_p = 0.0169, R_{wp} = 0.025, R_{F^2} = 0.0226, 2041 observations (1.36 Å D20) R_p = 0.041, R_{wp} = 0.0524, R_{F^2} = 0.0423, 233 observations (2.82 Å E9) R_p = 0.0291, R_{wp} = 0.0383, R_{F^2} = 0.0292, 885 observations (1.80 Å E9)	R_p = 0.036, R_{wp} = 0.0467, R_{F^2} = 0.0499, 1539 observations (1.80 Å) R_p = 0.0468, R_{wp} = 0.060, R_{F^2} = 0.0642, 416 observations (2.82 Å)
No. of observations	3949 for 6018 data points	1955 for 3586 data points
No. of parameters	163	101
No. of restraints	0	0

absences, $Pc2_1n$ (space group 33) and *Pcmn* (space group 62). As *Pcmn* is one of the minimal non-isomorphic super groups of $Pc2_1n$, the atomic positions refined from the $Pc2_1n$ triple cell model were inspected for equivalence caused by the missing symmetry operations. This allowed construction of a simplified model, which was also converted to the standard *Pnma* setting, containing 13 atoms in the asymmetric unit. Refinement using the four NPD datasets converged rapidly without the requirement for soft constraints on the bond lengths and angles, a significant improvement on the initial $Pc2_1n$ model. In the final cycles of the refinement, all atoms except phosphorus (which is in a regular tetrahedral geometry) were refined with anisotropic ADPs and CuO was refined as an impurity phase to 4.77 (1) wt %. The final Rietveld profile fit is given in Fig. 2 to the E9 1.80 Å data, derived interatomic distances and bond angles in Table 2 and the structure is illustrated in Fig. 3. Difference plots with fit statistics for each of the other datasets, Rb atom bond lengths and full bond-valence sum tables with different bond-length cutoffs for Rb are given in the supplementary material and the atomic positions in the supplied CIF.[1]

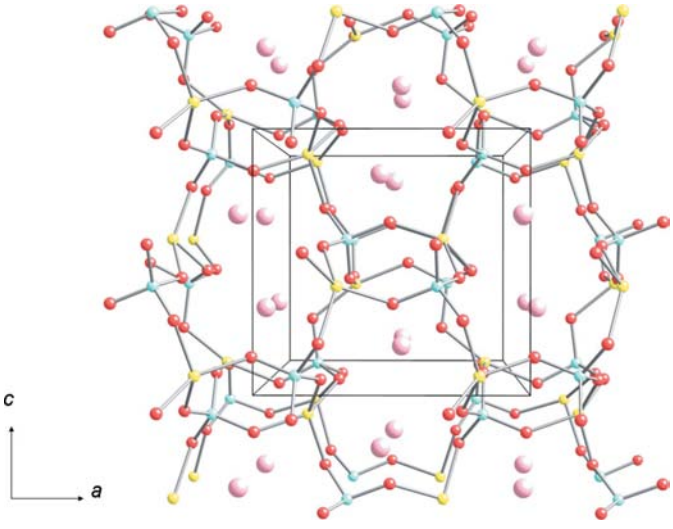

Figure 3
Structure of $RbCuPO_4$ (I) viewed just off the *ac* plane showing the eight-ring channels. The Cu atoms are yellow, the phosphorus light blue, the rubidium pink and the oxygen red. The black lines represent the unit cell.

[1] Supplementary data for this paper are available from the IUCr electronic archives (Reference: KD5046). Services for accessing these data are described at the back of the journal.

Table 2
Interatomic distances and bond angles for the copper and phosphorus polyhedra in $RbCuPO_4$ polymorph (I).

Cu1—O3	1.922 (4)	O3—Cu1—O5	163.0 (2)
Cu1—O5	1.945 (4)	O3—Cu1—O7 ×2	90.86 (10)
Cu1—O7 ×2	1.925 (2)	O5—Cu1—O7 ×2	91.39 (10)
Cu2—O1	1.965 (3)	O7—Cu1—O7	164.7 (2)
Cu2—O2	1.953 (3)	O1—Cu2—O2	96.39 (14)
Cu2—O4	1.889 (3)	O1—Cu2—O4	93.76 (13)
Cu2—O6	1.948 (3)	O1—Cu2—O6	138.92 (13)
P1—O2 ×2	1.549 (3)	O2—Cu2—O4	141.11 (11)
P1—O3	1.551 (5)	O2—Cu2—O6	91.29 (13)
P1—O5	1.516 (5)	O4—Cu2—O6	105.10 (12)
P2—O1	1.531 (3)	O2—P1—O2	108.0 (3)
P2—O4	1.540 (4)	O2—P1—O3 ×2	110.3 (2)
P2—O6	1.548 (4)	O2—P1—O5 ×2	108.8 (2)
P2—O7	1.538 (3)	O3—P1—O5	110.5 (3)
O1—P2—O4	108.3 (2)	O1—P2—O6	109.5 (2)
O1—P2—O7	108.4 (2)	O4—P2—O6	108.5 (2)
O4—P2—O7	111.76 (19)	O6—P2—O7	110.2 (2)

Table 3
Interatomic distances and bond angles for the copper and phosphorus polyhedra in $RbCuPO_4$ polymorph (II).

Cu1—P1	2.677 (9)	O1—Cu1—O2	71.1 (3)
Cu1—O1	1.957 (8)	O1—Cu1—O4	93.3 (3)
Cu1—O2	2.131 (8)	O1—Cu1—O7	162.6 (4)
Cu1—O3	2.183 (9)	O2—Cu1—O4	149.6 (4)
Cu1—O4	1.963 (8)	O2—Cu1—O7	94.7 (4)
Cu1—O7	1.888 (8)	O4—Cu1—O7	94.6 (4)
Cu2—O2	1.918 (8)	O2—Cu2—O5	144.8 (4)
Cu2—O6	1.959 (8)	O2—Cu2—O6	98.9 (4)
Cu2—O6	1.912 (8)	O2—Cu2—O8	95.4 (3)
Cu2—O8	1.925 (9)	O5—Cu2—O6	92.5 (3)
P1—O1	1.568 (9)	O5—Cu2—O8	95.5 (4)
P1—O2	1.563 (9)	O6—Cu2—O8	142.2 (4)
P1—O3	1.505 (10)	O1—P1—O2	99.0 (5)
P1—O4	1.503 (9)	O1—P1—O3	113.3 (6)
P2—O5	1.515 (9)	O1—P1—O4	113.1 (6)
P2—O6	1.556 (9)	O2—P1—O3	111.5 (6)
P2—O7	1.542 (11)	O2—P1—O4	108.0 (7)
P2—O8	1.544 (8)	O3—P1—O4	111.2 (7)
O5—P2—O6	106.3 (5)	O5—P2—O7	113.8 (6)
O5—P2—O8	111.3 (6)	O6—P2—O7	109.5 (5)
O6—P2—O8	107.7 (6)	O7—P2—O8	108.1 (6)

Table 2 shows that the P1 and P2 sites are tetrahedrally coordinated with bond lengths and angles well within those commonly seen for P^{5+} in this geometry. The bond-valence sums (BVSs) are 4.91 and 4.93. For each PO_4 unit, the tetrahedra share only vertices with the adjacent copper polyhedra. The rubidium cations lie within the large channels formed by the copper and phosphorus polyhedra and each has an irregular coordination. Rb1 is formally nine-coordinate with bond lengths varying from 2.843 (5) to 3.336 (3) Å and a BVS of 1.23, while Rb2 is eight-coordinate with bond lengths varying from 2.816 (3) to 3.226 (3) Å and a BVS of 1.17 (see supplementary material for further discussion on BVS calculations for rubidium). Cu1 is four-coordinate in almost square-planar geometry with the in-plane angles very close to 90°, giving a BVS of 2.03. However, the diagonal angles are less than 180°, as the refined Cu1 position is slightly out of plane formed by the four O atoms. Cu2 forms a typical Jahn–Teller distorted flattened tetrahedron with a BVS of 1.99 where the average in-plane bond angles are significantly distorted from the ideal 109° and the diagonal angles have reduced to around 140° from 180°. The ratio of Cu2:Cu1 is 2:1. All of the O atoms have bond contributions from one phosphorus, one copper and either one or two rubidium atoms in order to satisfy the valence requirements. The origin and importance of the differences in the copper coordination geometries and their effects on the observed structures will become clear when (I) is compared with (II).

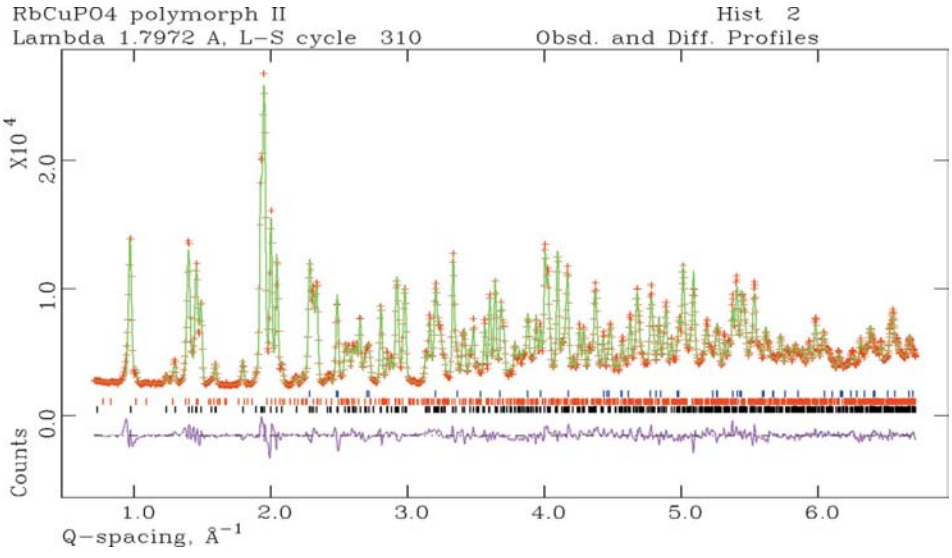

Figure 4
Final Rietveld refinement profile for the 1.80 Å incident wavelength E9 NPD data for $RbCuPO_4$ polymorph (II). The observed data are crosses, the calculated pattern a solid line, the tick marks show the allowed reflections [upper polymorph (I), middle CuO and lower polymorph (II)] and the lower solid line is the difference plot; R_{wp} = 0.0467, R_p = 0.0360 and R_{F^2} = 0.0499 for 1539 observations.

2.3. Structure of polymorph (II)

Many monoclinic variations of the ABW structure are known (Kahlenberg *et al.*, 2001) and so Le Bail type intensity extractions were performed using all of the possible primitive monoclinic space groups for the NPD data. Of these, $P2_111$ was found to give the best fit. However, it was not possible to rule out the presence of an inversion centre from the powder data alone due to the presence of impurity phases [(I) and CuO] and peak overlap of the *hkl* and $\overline{hkl}$ reflections. The result of the additional inversion symmetry would either be a disordered framework with an identical unit cell or an ordered framework with a doubled unit cell in one direction, as seen for

$CsCoPO_4$ (Henry, Hughes & Weller, 2000) and $CsZnPO_4$ (Blum *et al.*, 1986). A literature search of similar materials revealed that single crystals of $KCuPO_4$ had been grown and solved in the standard setting of the space group $P12_11$, with a similar unit cell (Shoemaker *et al.*, 1980). As single-crystal reflection statistics can distinguish the presence or lack of the inversion centre, the $P12_11$ model was used as a starting point for the Rietveld analysis of the multi-wavelength NPD data.

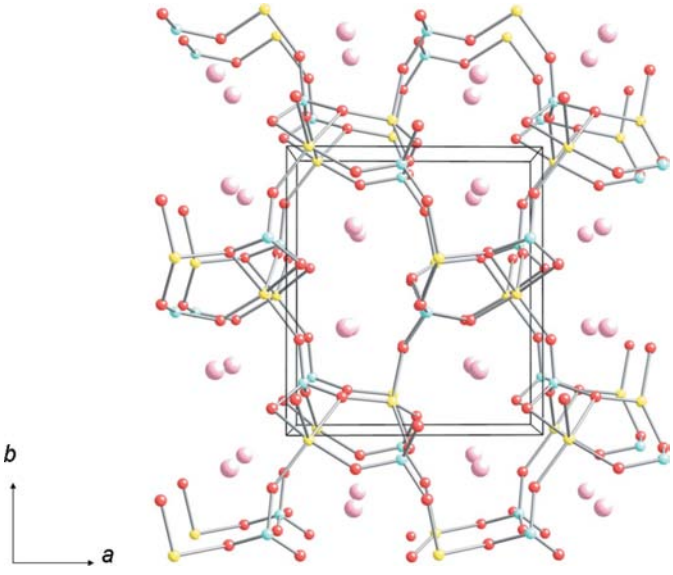

Figure 5
Structure of $RbCuPO_4$ (II) viewed just off the *ab* plane in order to illustrate the eight-ring channels as seen in Fig. 3. The different coordination geometries of the copper sites are clearly visible. The Cu atoms are yellow, the phosphorus light blue, the rubidium pink and the oxygen red. The black lines represent the unit cell.

The refinements converged rapidly with isotropic ADPs on all atoms with the presence of two minority phases [CuO at < 2 wt % and (I) at 5.89 (3) wt%]. Attempts to refine anisotropic ADPs led to better overall fit statistics but gave a significant number of non-positive definite displacement ellipsoids and therefore the structure is presented with isotropic ADPs in the supplied CIF. The final Rietveld profile fit is given in Fig. 4 to the E9 1.80 Å data, derived interatomic distances and bond angles in Table 3, and the structure is illustrated in Fig. 5. Difference plots with fit statistics for the other dataset, Rb atom bond lengths and full BVS tables are given as supplementary material.

The precision of the refinement for (II) is significantly lower than that for (I). However, the global structural features remain clear and mirror those found for the published $KCuPO_4$ single-crystal analogue. P1 has distorted tetrahedral geometry due to sharing an edge with Cu1, giving a short P1—Cu1 interatomic distance of 2.677 (9) Å. Despite the distortion, the P1 BVS (4.84) is reasonable for P^{5+}. P2 is a much more regular tetrahedron, only sharing vertices with the adjacent copper polyhedra, with a BVS of 4.77. As found in (I), Rb1 and Rb2 have irregular coordination geometries. Both sites are significantly overbonded from the BVS calculations at 1.32 and 1.14, primarily as a result of the range in bond lengths of 2.710 (8)–3.200 (9) Å for Rb1 and 2.779 (8)–3.657 (10) Å for Rb2 (see supplementary material for further discussion on BVS calculations for rubidium). If both sites are taken to be six-coordinate (cutoff of 3.15 Å in bond length) then the values become 1.15 and 1.05, although six-fold coordination is lower than that usually reported for the larger group (I) metals. Cu1 is five-coordinate in a significantly distorted square-based pyramidal arrangement, where the 5th Cu—O contact is formed by a rotation of the adjacent P1

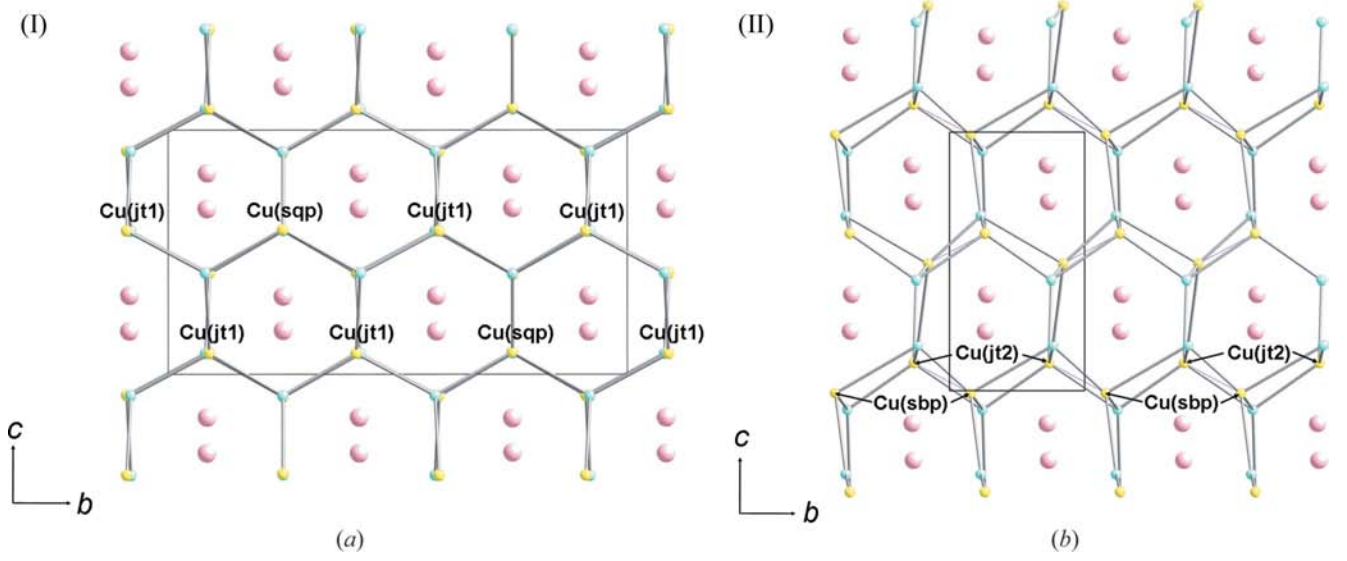

Figure 6
Topological representation of the structure of (*a*) (I) and (*b*) (II) viewed perpendicular to the six-ring planes. In (I) each layer has 2 × Cu(jt1) and 1 × Cu(sqp) making up the six-ring that is rotated by 180° in the plane above and below yielding a regular honeycomb channel. In (II) each six-ring layer is composed of a single type of copper site and a short Cu(sbp)—Cu(jt2) interlayer distance results, shown as dashed lines, yielding irregular six-ring channels. The Cu atoms are yellow, the phosphorus light blue, the rubidium pink and the oxygen red. The black lines represent the unit cell.

tetrahedron such that O2 is shared between two copper and one phosphorus polyhedra. The BVS of 2.06 is also reasonable. Cu2 forms a typical Jahn–Teller distorted flattened tetrahedron with a BVS of 2.04, similar to that found for Cu2 in (I). With the exception of O2, all of the O atoms have bond contributions from one phosphorus, one copper and either one or two rubidium atoms. This satisfies the valence requirements for all of the atoms except O3 whose sum is a little low at 1.87 as in $KCuPO_4$.

3. Discussion

Comparing the unit cells of (I) and (II), it is not immediately obvious how the structures are related. In order to compare the site types from the two polymorphs, a new naming scheme will be adopted for the discussion. In (I) the Cu1 site becomes Cu(sqp), to reflect the approximate square-planar nature of the coordination sphere, and Cu2 becomes Cu(jt1), for the Jahn–Teller distorted tetrahedron. In (II) the Cu1 and Cu2 sites are renamed Cu(sbp) and Cu(jt2) as the first site is a square-based pyramid (five-coordinate) and the second site is a Jahn–Teller distorted tetrahedron (four-coordinate) like that in (I).

Both materials are based on the $4^2 6^3 8$-*a* network (Smith, 1977; Wells, 1979) observed for zeolite ABW (Kerr, 1974). This is one of several four-connected networks that can be constructed by allowing a tetrahedral point to make three connections within a layer and the fourth to an adjacent layer (Feng *et al.*, 1997). To determine the topology type, the copper and phosphorus are directly linked (disregarding the oxygen) to provide a simplified picture, and this gives rise to four-, six- and eight-ring channels, each aligned with one of the crystallographic directions. The clearest way to visualize the $4^2 6^3 8$-*a* network is to view perpendicular to the six-ring sheets (made up of alternating copper and phosphorus polyhedra so that each ring has three Cu and three P atoms) illustrated in Fig. 6

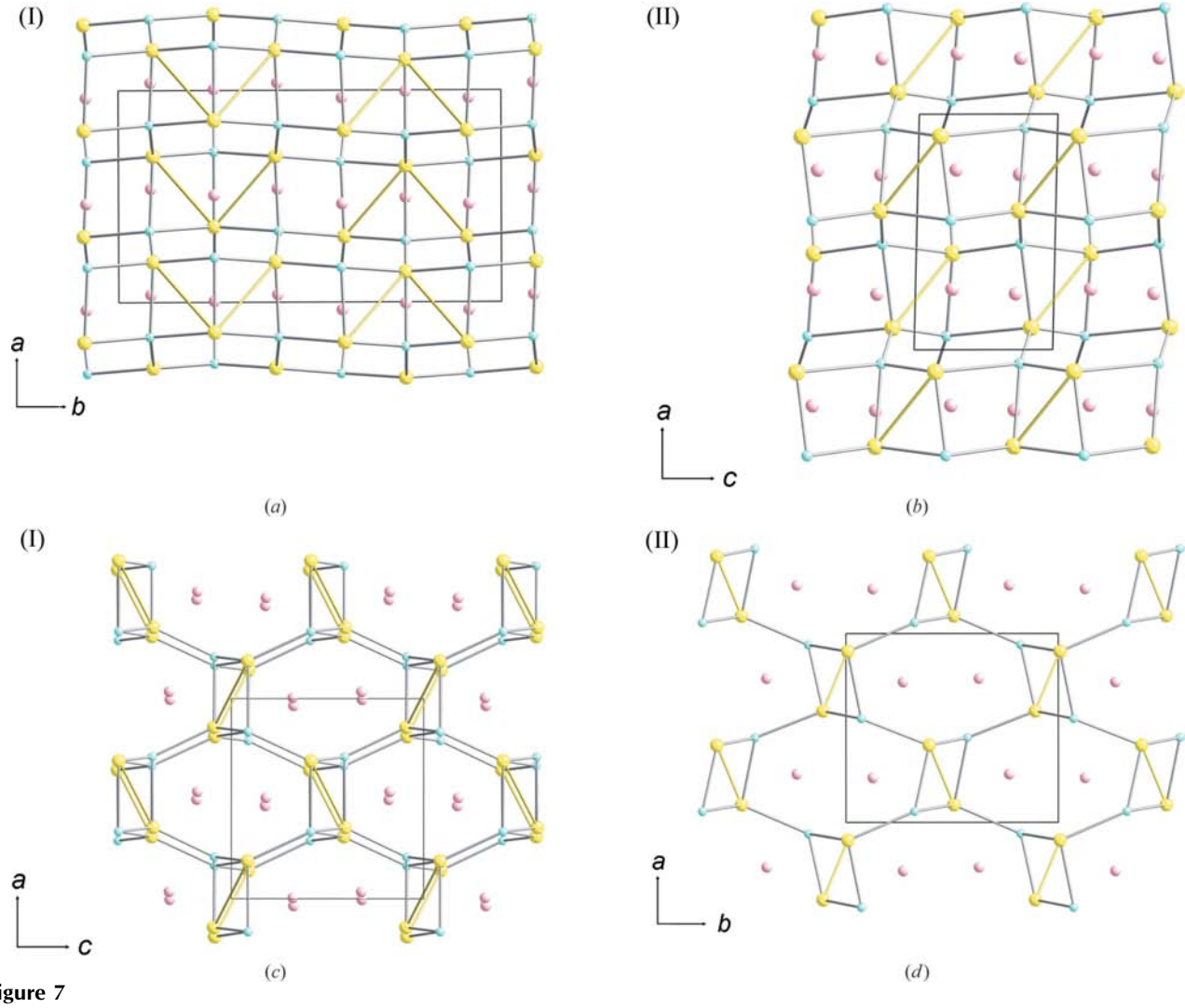

Figure 7
Topological view of the structures of (*a*) and (*c*) (I), and (*b*) and (*d*) (II) viewed perpendicular to the four-ring (upper) and eight-ring (lower) planes. The difference in the periodicity in the four-ring plane is particularly evident. The short Cu—Cu distances are marked as solid yellow cylinders in each case, giving the trimer units in (I) and the dimer units in (II) as described in the text. The Cu atoms are yellow, the phosphorus light blue and the rubidium pink. The black lines represent the unit cell.

for each polymorph. In (I) (Figs. 6*a* and *c*) two of the copper sites within each six-ring are Cu(jt1) type and the third is Cu(sqp) type. Taking a single vertex of the six-ring shows that the site type when translating along **b** is Cu(jt1), Cu(jt1), Cu(sqp), Cu(jt1), Cu(jt1), Cu(sqp) *etc*. This explains the tripling of **b** compared with the original unit cell and the relatively small difference in the copper coordination polyhedra (both are four-coordinate and intermediate between tetrahedral and square-planar geometry) and accounts for the fact that the tripling was missed in the initial analysis of the XPD data. The subsequent six-ring layer has the copper and phosphorus sites interchanged, giving regular alternating layers with a 2:1 ratio of copper-site type with an almost perfect honeycomb channel parallel to **a**. In (II) (Figs. 6*b* and *d*) the six-ring layers are buckled in order to accommodate the five-coordinate copper site. This gives rise to alternating layers composed uniquely of each type of copper site, *i.e.* a layer with three Cu(sbp) containing six-rings above a layer of three Cu(jt2) containing six-rings. This also explains the mismatch in the multiplicity of the copper sites between the two refined structures. In the perfect case there would be a single copper site describing both layers resulting in topologically identical sheets as found in $KNiPO_4$.

Fig. 7 shows the topological structure of (I) and (II) in the eight-ring direction (left) and four-ring directions (right) in order to illustrate how the copper coordination gives rise to each structure type and also to illustrate the secondary structural characteristics described below. It can be seen that while (I) has almost perfect honeycomb channels in the six-ring direction, this causes a corrugation between the layers in the eight-ring direction and the formation of Cu trimers that contain a mirror plane in the four-ring directions, with Cu(jt1)—Cu(sqp) distances of 2 × 4.212 (7) Å. These trimers alternate in an up and down manner along **b** such that the

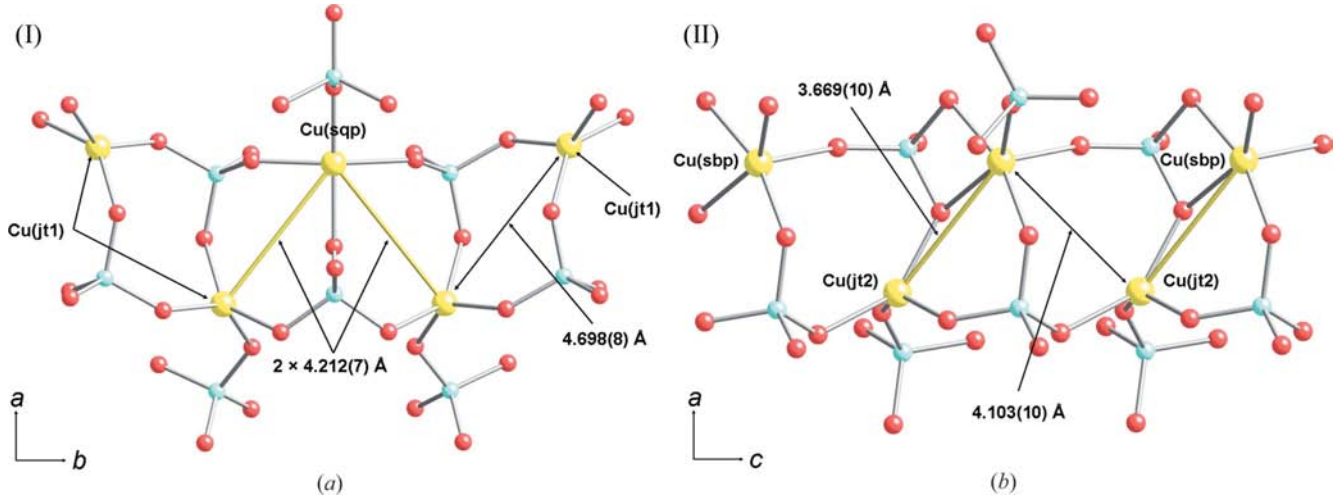

Figure 8
Structural view of the trimer Cu units in (*a*) (I) and the dimer Cu units in (*b*) (II) viewed perpendicular to the four-ring plane. Polymorph (II) is generated from (I) *via* a rotation of a phosphate group to generate a fifth contact to the square-planar Cu site (centre of the trimer) in (I), which breaks the mirror symmetry. The Cu atoms are yellow, the phosphorus light blue and the oxygen red. Rb atoms are not shown for clarity.

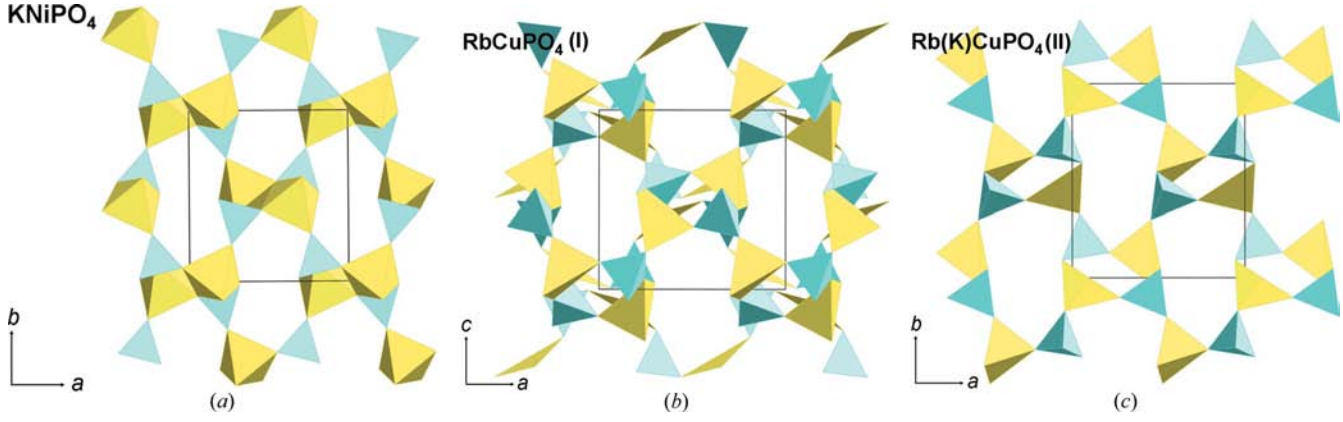

Figure 9
Polyhedral view of (*a*) KNiPO4, (*b*) (I) and (*c*) (II)/$KCuPO_4$ illustrating the ordering of the phosphate groups in the chains parallel to the eight-ring direction. Only $KNiPO_4$ and (II) show phosphate chains parallel to the eight-ring direction that are in-register. The difference in the directions of the phosphate groups in the next nearest-neighbour chains is also evident for KNiPO4 and (II). Phosphate polyhedra are blue and copper polyhedra are yellow.

Cu(jt1)—Cu(jt1) intertrimer distance is 4.698 (7) Å. In the perpendicular direction (along **a**), the trimers form Vs that are in register, with intertrimer nearest Cu(jt1)—Cu(sqp) distances of 2 × 5.256 (8) Å and a longest intratrimer Cu(jt1)—Cu(jt1) distance of 5.155 (8) Å. The buckling of the six-ring sheets in (II) in order to accommodate the five-coordinate copper site gives rise to one short and one long interlayer Cu(jt2)—Cu(sbp) distance of 3.668 (10) and 4.097 (10) Å. This results in the formation of one-dimensional chains of paired copper polyhedra running parallel to the **a** direction in (II), marked as solid yellow cylinders in the figure, yielding interesting magnetic properties that will be reported elsewhere. Fig. 8 illustrates the local copper environment, highlighting the difference between the two polymorphs. It is clear that rotation of one of the phosphate groups in (I) breaks the mirror symmetry of the trimer group in order to form the fifth Cu—O bond. The flexibility of the three-dimensional structure then allows a relaxation to propagate this symmetry breakage through the crystal structure, yielding the dimer structure.

Shoemaker *et al.* (1980) also rationalized the relationship between the structure of $KCuPO_4$ and that of $KNiPO_4$ in terms of packing vertex-sharing chains in a hexagonal close packed (h.c.p.) array. In $KNiPO_4$ all of the nickel sites are five-coordinate, whereas in $KCuPO_4$ and $RbCuPO_4$ (II) there are four- and five-coordinate Cu in a 1:1 ratio. In (II) if Cu(jt2) forms a fifth bond to O7 then it becomes topologically equivalent to Cu(sbp) by sharing an edge with P2 and yields the $KNiPO_4$ structure type. In addition, each copper polyhedron would share two vertices with adjacent copper polyhedra to form chains parallel to **c**. The phosphate tetrahedra then share one edge and a vertex with copper polyhedra within the chain, with the fourth vertex the attachment for neighbouring chains. Examination of the structure of (II) shows that all of the phosphate tetrahedra point in the same direction (± **c**) within a chain, while the adjacent chains point in the opposite direction. The chains are symmetrically related by the 2_1 axis along **b**. The basic difference between $KNiPO_4$ and $KCuPO_4$ [RbCuPO4, (II)] is the orientation of the 2_1 axis. In the former it lies parallel to the chains, whereas in the latter it lies perpendicular to the chains. As a result, all of the phosphate tetrahedra point in the same direction in $KNiPO_4$, while $KCuPO_4$ and (II) have phosphate groups in adjacent chains that point in opposite directions. In (I) the ordering of the phosphate groups is much more complex and there are no longer chains of PO_4 tetrahedra that point in the same direction perpendicular to the eight-ring direction (±**b** in the *Pnma* structure), shown in Fig. 9. The difference between the chains in $KCuPO_4$ and $KNiPO_4$ is related to the arrangement of the interstitial positions in the h.c.p. array as detailed by Shoemaker *et al.* (1980). In (I) the formation of the copper trimer units add a further degree of complexity to this chain description of the structure, which is reflected in the non-simple orientation of the phosphate groups in Fig. 9. This suggests that there are many subtle structural variations possible within phosphates based on the $4^2 6^3 8$-*a* topological network and that the choice of counter cation and transition metal are crucial in deciding which types of ordering are observed.

The driving force for the (II) → (I) phase transition under grinding and full conversion under the application of 5 tonnes pressure by pelletization seems, at first sight, counter-intuitive. Polymorph (I) contains only four-coordinate copper sites, whereas (II) contains four- and five-coordinate copper sites. Usually, under applied pressure, coordination numbers increase. However, the ordering of the six-ring sheets and copper trimer formation observed in (I) leads to a significant contraction of almost 2.1% in the volume of the basic unit cell [411.09 (4) *versus* 419.84 (2) $Å^3$]. The colour change in the material is also evidence of a change in coordination environment of the active centres, in this case copper. $KCuPO_4$, which has the same structure type as (II), is also reported to be a very pale green powder. The sky blue colour observed for (I) is consistent with that expected for purely four-coordination of Cu to O atoms (Hathaway & Billing, 1970).

There is also a rich phase field in this quaternary material as a function of temperature cycling as a result of the room-temperature polymorphism, but it is outside the scope of this initial structural manuscript and will be published elsewhere. As stated above, the nature of the dimerization of the copper sites to form one-dimensional chains in (II) gives rise to significant differences in the magnetic properties of the polymorphs, which will also be detailed elsewhere.

4. Conclusions

Polymorphism has been shown to occur in $RbCuPO_4$, generated by subtle interplay between the copper and phosphate coordination polyhedra. Polymorph (I) has an orthorhombic structure (*Pnma*) containing two different four-coordinate copper centres in a 2:1 ratio, centres that form trimer chains giving a complex array of phosphate groups in three dimensions, based on the $4^2 6^3 8$-*a* network. Polymorph (II) crystallizes in the known $KCuPO_4$ monoclinic ($P2_1$) variant of the $4^2 6^3 8$-*a* network containing a 1:1 ratio of four- and five-coordinate copper sites giving an ordered array of phosphate group chains parallel to the *c* direction. Polymorph (II) also contains dimers of copper polyhedra parallel to the **a** direction (in the 4-ring plane), dimers that yield interesting magnetic properties as a result of breaking the mirror symmetry of the trimeric copper moieties in (I). The (II) → (I) phase transition under grinding pressure is driven by a contraction in the basic unit-cell volume, even though the average coordination number of the copper falls. The observation of polymorphism in $RbCuPO_4$, controlled by the application of pressure and the cooling regime, and that the two polymorphs can co-exist under ambient conditions suggest that $RbCuPO_4$ sits right at a boundary of stability and that the preferred structure type could be controlled by doping either the *A* site (Rb) or the *B* site (Cu) in $RbCuPO_4$. It also hints at a route to control the dimensionality of the magnetism, a route which is being actively pursued.

We would like to thank the Helmholtz Zentrum Berlin and the Institut Laue Langevin for the neutron beamtime presented in this manuscript under proposals CHE-01-2593 and 5-24-231 respectively.

References

Baerlocher, Ch. & McCusker, L. B. (1996). *Database of Zeolite Structures*, http://www.iza-structure.org/databases/.
Blum, D., Durif, A. & Averbuch-Pouchot, M. T. (1986). *Ferroelectrics*, **69**, 283–292.
Bu, X. H., Feng, P. Y., Gier, T. E. & Stucky, G. D. (1997). *Zeolites*, **19**, 200–208.
Cheong, S.-W. & Mostovoy, M. (2007). *Nature Mater.* **6**, 13–20.
Chippindale, A. M., Cowley, A. R., Chen, J., Gao, Q. & Xu, R. (1999). *Acta Cryst.* C**55**, 845–847.
Corbridge, D. E. C. (1973). *The Structural Chemistry of Phosphorus*, p. 85. New York: Elsevier.
Eerenstein, W., Mathur, N. D. & Scott, J. F. (2006). *Nature*, **442**, 759–765.
Feng, P. Y., Bu, X. H., Tolbert, S. H. & Stucky, G. D. (1997). *J. Am. Chem. Soc.* **119**, 2497–2504.
Hansen, T. C., Henry, P. F., Fischer, H. E., Torregrossa, J. & Convert, P. (2008). *Meas. Sci. Technol.* **19**, 034001.
Harrison, W. T. A. (2000). *Z. Kristallogr.* **215**, 288–292.
Hathaway, B. J. & Billing, D. E. (1970). *Coord. Chem. Rev.* **5**, 143–207.
Henry, P. F., Hughes, R. W., Ward, S. C. & Weller, M. T. (2000). *Chem. Commun.* pp. 1959–1960.
Henry, P. F., Hughes, E. M. & Weller, M. T. (2000). *J Chem. Soc. Dalton Trans.* pp. 555–558.
Henry, P. F., Weller, M. T. & Hughes, R. W. (2000). *Inorg. Chem.* **39**, 5420–5421.
Jensen, T. B. S., Christensen, N. B., Kenzelmann, M., Rønnow, H. M., Niedermayer, C., Andersen, N. H., Lefmann, K., Jiménez-Ruiz, M., Demmel, F., Li, J., Zarestky, J. L. & Vaknin, D. (2009). *Phys. Rev. B*, **79**, 092413.
Jensen, T. B. S., Christensen, N. B., Kenzelmann, M., Rønnow, H. M., Niedermayer, C., Andersen, N. H., Lefmann, K., Schefer, J., von Zimmermann, M., Li, J., Zarestky, J. L. & Vaknin, D. (2009). *Phys. Rev. B*, **79**, 092412.
Kahlenberg, V., Fischer, R. X. & Baur, W. H. (2001). *Z. Kristallogr.* **216**, 489–494.
Kerr, I. S. (1974). *Z. Kristallogr.* **139**, 186–195.
Khomskii, D. I. (2006). *J. Magn. Magn. Mater.* **306**, 1–8.
Larson, A. C. & Von Dreele, R. B. (1994). *GSAS*, Report LAUR 86–748. Los Alamos National Laboratory, New Mexico, USA.
Mo, X. H., Etheredge, K. M. S., Hwu, S. J. & Huang, Q. (2006). *Inorg. Chem.* **45**, 3478–3480.
Ranmohotti, K. G. S., Mo, X. H., Smith, M. K. & Hwu, S. J. (2006). *Inorg. Chem.* **45**, 3665–3670.
Shoemaker, G. L., Kostiner, E. & Anderson, J. B. (1980). *Z. Kristallogr.* **152**, 317–332.
Smith, J. V. (1977). *Am. Mineral.* **62**, 703–709.
Többens, D. M., Stüßer, N., Knorr, K., Mayer, H. M. & Lampert, G. (2001). *Mater. Sci. Forum*, **378–381**, 288–293.
Toby, B. H. (2001). *J. Appl. Cryst.* **34**, 210–213.
Vaknin, D., Zarestky, J. L., Rivera, J.-P. & Schmid, H. (2004). *Phys. Rev. Lett.* **92**, 207201.
Weller, M. T. (2000). *J. Chem. Soc. Dalton Trans.* pp. 4227–4240.
Wells, A. F. (1979). *Further Studies of Three-Dimensional Nets.* ACA Monograph No. 8, p. 35.